



Modeling of liquid-solid hydrodynamic water wave energy harvesting system based on triboelectric nanogenerator[☆]

Xuemei Zhang^a, Qianxi Yang^a, Peiyuan Ji^a, Zhifei Wu^a, Qianying Li^a, Huake Yang^a, Xiaochuan Li^a, Guocan Zheng^a, Yi Xi^{a,*}, Zhong Lin Wang^{b,c,**}

^a Chongqing Key Laboratory of Soft Condensed Matter Physics and Smart Materials, Department of Applied Physics, Analytical and Testing Center, Chongqing University, Chongqing 400044, PR China

^b Georgia Institute of Technology, Atlanta, GA 30332, USA

^c Beijing Institute of Nanoenergy and Nanosystems, Chinese Academy of Sciences, Beijing 100083, PR China

ARTICLE INFO

Keywords:

Triboelectric nanogenerator
Water wave
Hydrodynamic modeling
Self-powered smart agriculture

ABSTRACT

Wave energy collector (WEC) based on triboelectric nanogenerator (TENG) (W-TENG) is excellent candidate in complex marine environments. However, the improvement of energy conversion efficiency and understanding of motion mechanisms of W-TENG were limited due to the lack of theoretical basis. Here, based on the theory of hydromechanics, an energy conversion model is proposed to unveil the energy conversion mechanism and interaction mechanism between W-TENG (solid) and water wave (liquid) during the wave energy harvesting process. An inverted pendulum-typed multilayer triboelectric nanogenerator (IPM-TENG) is developed to capture water wave energy in weak wave environment (wave height: 2–13 cm, wave frequency: 0.5–1.25 Hz). Guided by the theoretical model and hydrodynamic experiments, the structural parameters and output performance of the device are further optimized. Most importantly, the available energy conversion efficiency of the optimized device is up to 14.5%. Furthermore, the optimized IPM-TENG can serve as a console for the ‘on demand’ release of pesticides to promote the development of self-powered smart agriculture. This work can not only provide guidance for the design and energy conversion efficiency improvement of future blue energy harvesting devices, but also accelerate the commercial rollout and practical application of W-TENG.

1. Introduction

Liquids in nature have enormous energy, and the ocean energy with huge quantity is one of the most sustainable energy sources, which is expected to be developed and applied on a large scale [1–3]. Despite decades of exploration, the current water wave energy harvesting schemes are still insufficient [4–8].

Triboelectric nanogenerator (TENG), derived from Maxwell's displacement current, is based on the coupling of triboelectric electrification and electrostatic induction [9–15]. Because the merits of efficient conversion of irregularly distributed ambient mechanical energy into electrical energy, lightweight, low cost, diverse materials and structures, TENG exhibits overwhelming advantages over

electromagnetic generator (EMG) for the collection of low-frequency ocean wave energy [16–18]. So far, TENG with various structures and working mechanisms have been developed to harvest water wave energy according to the characteristics of waves [19–21]. And recently, Xu et al. experimentally studied the interaction between W-TENG with different shape characteristics and water waves [22]. Wang et al. studied the hydrodynamic characteristics of W-TENG under different structural parameters and wave conditions through experimental tests and software simulations [23]. However, the mechanism of the coupling between the W-TENG and the water wave includes the dynamic process and the corresponding energy conversion mechanism has been seldom studied in theory [24–27].

In this work, an energy conversion model is built based on the theory

[☆] Prof Zhong Lin Wang, an author on this paper, is the Editor-in-Chief of Nano Energy, but he had no involvement in the peer review process used to assess this work submitted to Nano Energy. This paper was assessed, and the corresponding peer review managed by Professor Chenguo Hu, also an Associate Editor in Nano Energy

* Corresponding author.

** Corresponding author at: Georgia Institute of Technology, Atlanta, GA 30332, USA.

E-mail addresses: yxi6@cqu.edu.cn (Y. Xi), zhong.wang@mse.gatech.edu (Z.L. Wang).

<https://doi.org/10.1016/j.nanoen.2022.107362>

Received 20 March 2022; Received in revised form 29 April 2022; Accepted 5 May 2022

Available online 10 May 2022

2211-2855/© 2022 Elsevier Ltd. All rights reserved.

of hydromechanics (linear wave theory and Morison equation), which specifies the dynamic process of the interaction between the W-TENG (solid) and the water wave (liquid fluid), and the corresponding energy conversion mechanism. Taking the inverted pendulum-typed multilayer TENG (IPM-TENG) as an example, the model successfully calculated the motion trajectory and captured energy of the IPM-TENG during the interaction with the water wave. Under different structural parameters and wave conditions, the captured available energy calculated by the model has the same trend of variation as the electric energy obtained by the IPM-TENG in the actual water wave. The optimized device has an average power of 0.845 mW with an external load of 5 MΩ and an energy conversion efficiency of 14.5% has been demonstrated. In addition, by harvesting ocean energy, IPM-TENG can be used to control the pesticide release and build self-powered smart agricultural systems. The proposed theoretical model can effectively assist the design and optimization of future W-TENG, improve the energy conversion efficiency in process of water wave energy harvesting, and facilitate the commercial promotion and practical application of W-TENG.

2. Result and discussion

2.1. Structure and working mechanism

In the past, most studies focus on designing and optimizing the structure of water wave energy collector (WEC), so the interaction between the water wave (liquid fluid) and WEC (solid) need further study to understand the nature of wave energy harvesting. An energy conversion model was developed to investigate the underlined fundamental

science (Fig. 1a). Based on this model, the IPM-TENG, floating on the ocean surface, was designed and optimized for collecting water wave energy (Fig. 1b). Moreover, the controllable manner for releasing agrochemicals has the potential to transform conventional agricultural production systems. Fig. 1c illustrates that an IPM-TENG based controllable pesticide release system (ICPRS) is expected to build self-powered smart agriculture systems. For the practical wave energy harvesting, an efficient energy conversion model needs to be constructed, the framework of which is shown in Fig. 1d. First, the WEC vibrates with water waves, capturing the parts of mechanical energy of the water, with an energy transmission efficiency of η_1 . Second, the parts of captured energy by WEC transfer to available energy with an energy transfer efficiency of η_2 . Then, the moved WEC triggers the inner TENG units to work and output electric power, with mechanical to electrical conversion efficiency η_3 .

The IPM-TENG is composed of a floating body with four independent multilayered paper-based TENG units and an acrylic shell, an assist body, and a connecting rod linked the floating body and the assist body (Fig. 1e). As shown in Fig. 1f four independent multilayered TENG units inside the acrylic shell of the floating body are labeled as units 1–4, respectively. The insert of Fig. 1f shows the photographs of the as-fabricated IPM-TENG and the single TENG unit. Each multilayered TENG unit has three basic contact-separation mode units, and they are connected by ropes to ensure that they can all work effectively. The basic TENG unit is fabricated by paper as substrate, aluminum foil (Al, 30 μm) as electrodes, and polytetrafluoroethylene film (PTFE, 30 μm) as dielectric layer. The detailed fabrication process of TENG is displayed in the experimental section.

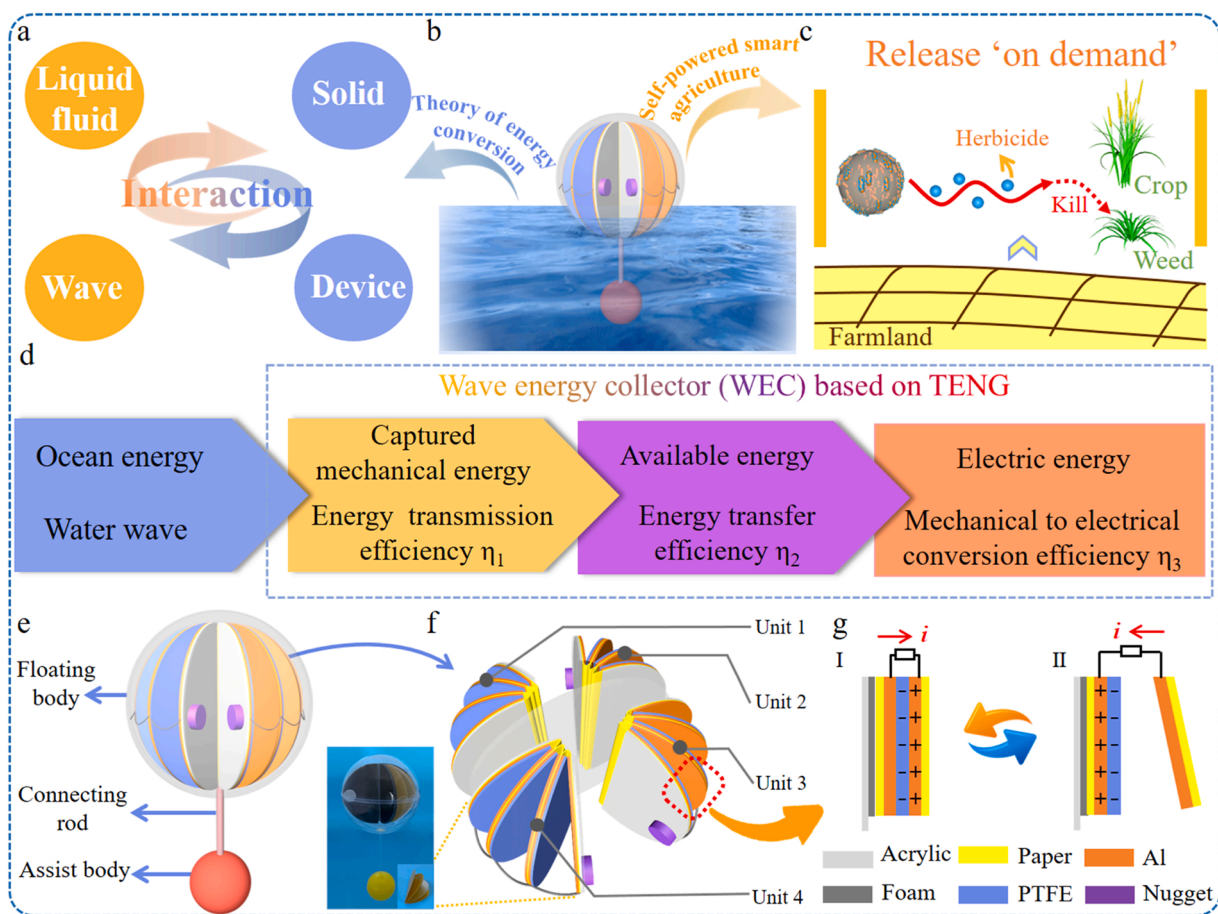


Fig. 1. Structural and working principle of the proposed IPM-TENG. The conceptual and effective mechanism diagram of IPM-TENG for (a) energy conversion mechanism modeling, (b) wave energy harvesting, and (c) herbicide release control. (d) Energy conversion model for the energy harvesting performance of wave energy collector. (e) The structure photography of IPM-TENG. (f) Exploded view of the TENG units. (g) The working mechanism of TENG unit.

When the water wave triggers the IPM-TENG, the nuggets on the outside of TENG units move due to inertia and drive the multilayered TENG units to work. The working principle of a basic TENG unit is depicted in Fig. 1g, which is based on the couple of triboelectric electrification and electrostatic induction effect. In the initial state, the dielectric PTFE film and the Al electrode in the right are contacted with each other. Due to the triboelectric effect, the PTFE film captures negative charges and the Al electrode in the right captures the same number of positive charges, respectively (Fig. 1g (I)). Under the act of wave, the PTFE film gradually separates with the Al film in the right, the potential difference between the two Al electrodes causes the electrons flowing from the Al electrode in the left to the right through the external circuit and generating a pulse current (Fig. 1g (II)). When the PTFE film gradually contacts with the Al film in the right, a reverse current will generate in the load. Therefore, when the water wave continuously drives the IPM-TENG to work, an alternating current (AC) output can be produced.

2.2. Hydrodynamic modeling

In the complex ocean environment, the collection of wave energy is great challenging [28]. The following problems are the obstacles

encountered in the process of structural design, for example, what are environmental loads subjected by the WEC, how does the WEC move in the wave condition, and what is the energy conversion mechanism in the energy harvesting process, and so on [29]. To solve those questions, an energy conversion model is built based on the linear wave theory and Morison equation.

Suppose the designed IPM-TENG has rigid body motion in the water wave with wave height of H , and wavelength of L . A coordinate system xyz satisfying the right-hand rule is defined with the origin point O at the projected position of the crest of the linear wave on the still water level (SWL, $z = 0$). The origin point O' of the $x'y'z'$ coordinate system is selected at the position of $(x_0, 0, 0)$ in the xyz coordinate system (Fig. 2a (I)). The center of gravity (COG) of the IPM-TENG, COG of the floating body, and COG of the assist body are defined as point C $(x_0, 0, z_0)$, point A $(x_1, 0, z_1)$, and point B $(x_2, 0, z_2)$, respectively (per unit time). The details are all illustrated in Fig. S1a. The relationship among the vectors of \vec{r}_{OA} , \vec{r}_{OC} , \vec{r}_{CA} , \vec{r}_{OB} and \vec{r}_{CB} (per unit time) can be described as

$$\vec{r}_{OA} = \vec{r}_{OC} + \vec{r}_{CA} \quad (1)$$

$$\vec{r}_{OB} = \vec{r}_{OC} + \vec{r}_{CB} \quad (2)$$

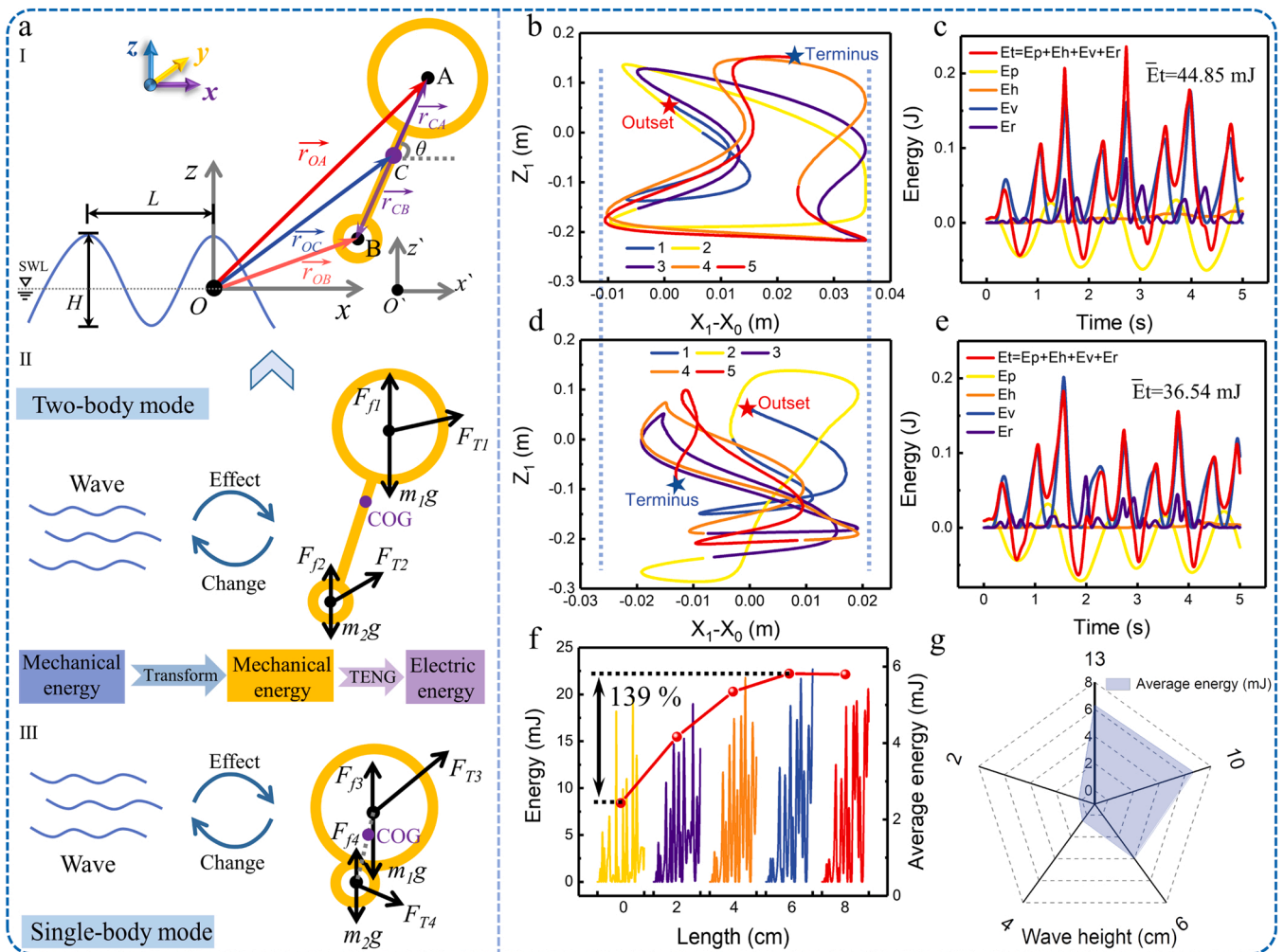


Fig. 2. Model construction and theoretical calculation of energy conversion mechanism. (a) Force analysis and principles of energy conversion of the two modes device in the wave. (b) The calculated trajectory of point A of the two-body mode in the xoy plane. (c) The details of captured energy (potential energy of the COG (E_p), translational kinetic energy of COG moving along the x -axis (E_h), translational kinetic energy of the COG moving along the z -axis (E_v), rotational kinetic energy (E_r), total energy (E_t)) of IPM-TENG in the two-body mode. (d) The calculated trajectory of point A of the single-body mode in the xoy plane. (e) The details of captured energy by IPM-TENG in the single-body mode. The available energy of the floating body and corresponding average energy with (f) different lengths of connecting rod (g) with different heights of wave.

the x and z components of the two Eqs. (1–2) can be written as

$$x_1 = x_0 + r_1 \cos\theta \quad (3)$$

$$z_1 = z_0 + r_1 \sin\theta \quad (4)$$

$$x_2 = x_0 - r_1 \cos\theta \quad (5)$$

$$z_2 = z_0 - r_1 \sin\theta \quad (6)$$

here r_1 and r_2 are the distance between point C and point A, and the distance between point C and point B, respectively. θ is the angle between the line of CA and the x -axis. Since the position of COG of any object is not affected by the state of motion, the state where the line AC of IPM-TENG is parallel to the x -axis is used to study the position of COG of the device.

$$m_1 g r_1 = m_2 g r_2 \quad (7)$$

$$r_1 + r_2 = r = a_1 + a_2 + l \quad (8)$$

where m_1 and m_2 are the mass of the floating body and the assist body, respectively. g is the gravitational acceleration, r is the distance between point A and B. a_1 and a_2 are the radius of the floating body and the assist body, respectively. l is the length of the connecting rod. Thus

$$r_1 = \frac{m_2(a_1 + a_2 + l)}{m_1 + m_2} \quad (9)$$

$$r_2 = \frac{m_1(a_1 + a_2 + l)}{m_1 + m_2} \quad (10)$$

For the energy conversion model, during the process of wave energy harvesting, the wave impacts the two modes of IPM-TENG, due to the relative motion and the viscosity between wave and IPM-TENG, wave loads \vec{F}_{T1} and \vec{F}_{T2} will generate on the floating body and assist body of IPM-TENG in the two-body mode, respectively (Fig. 2a (II)). Wave loads \vec{F}_{T3} and \vec{F}_{T4} will generate on the floating body and assist body of IPM-TENG in the single-body mode, respectively (Fig. 2a (III)). Here wave load refers to the resultant force of the drag force and inertial force on the research object exerted by the water wave. Those wave loads affect the state of IPM-TENG. In the meantime, the altered state and position of the IPM-TENG will change the wave distribution in turn. In the water wave energy harvesting process, the part of mechanical energy of water wave transfers to the IPM-TENG, and then the captured available mechanical energy of IPM-TENG triggers the inside TENG units, at last, the TENG converts the mechanical energy into usable electrical energy (Fig. 2 and Fig. S1).

According to the linear wave theory, temporal wave surface elevation $\eta(x, t)$ can be expressed as [30,31].

$$\eta(x, t) = \frac{H}{2} \cos(kx - \omega t) = \frac{H}{2} \cos\left(\frac{2\pi}{L}x - \omega t\right) \quad (11)$$

here H , k , L , and ω are the depth, number, length, and angular frequency of the wave, respectively. The relationship between ω , the period T , and wave frequency f can be described as:

$$f = \frac{1}{T} = \frac{\omega}{2\pi} \quad (12)$$

The corresponding velocity potential ϕ is

$$\phi = \frac{Hg}{2\omega} \frac{ch[k(z+d)]}{sh(kd)} \sin(kx - \omega t) \quad (13)$$

here d is the distance between the xoy plane and the seabed. The wave velocity (\vec{v}_w) and the corresponding x components of wave velocity (\vec{u}) and z components of wave velocity (\vec{v}) at a point (x, y, z) are

$$\vec{v}_w = \vec{u} + \vec{v} \quad (14)$$

$$\vec{u} = \frac{\partial\phi}{\partial x} = \frac{\pi H}{T} \frac{ch[k(z+d)]}{sh(kd)} \cos(kx - \omega t) \vec{i} \quad (15)$$

$$\vec{v} = \frac{\partial\phi}{\partial z} = \frac{\pi H}{T} \frac{sh[k(z+d)]}{sh(kd)} \sin(kx - \omega t) \vec{k} \quad (16)$$

where \vec{i} , and \vec{k} are the unit vectors in the x and z directions, respectively. The wave acceleration (\vec{v}_w) and the corresponding x components of wave acceleration (\vec{u}) and z components of wave acceleration (\vec{v}) at a point are:

$$\vec{v}_w = \vec{u} + \vec{v} \quad (17)$$

$$\vec{u} = \frac{du}{dt} = \frac{\partial u}{\partial t} + \frac{\partial u}{\partial x} u + \frac{\partial u}{\partial z} v \approx \frac{\partial u}{\partial t} = \frac{2\pi^2 H}{T^2} \frac{ch[k(z+d)]}{sh(kd)} \sin(kx - \omega t) \vec{i} \quad (18)$$

$$\vec{v} = \frac{dv}{dt} = \frac{\partial v}{\partial t} + \frac{\partial v}{\partial x} u + \frac{\partial v}{\partial z} v \approx \frac{\partial v}{\partial t} = \frac{2\pi^2 H}{T^2} \frac{sh[k(z+d)]}{sh(kd)} \cos(kx - \omega t) \vec{k} \quad (19)$$

Then use the Morison equation (per unit time) on the unconstrained research object [32,33].

$$\vec{F}_T = \vec{F}_D + \vec{F}_I \quad (20)$$

$$\vec{F}_D = \frac{\rho C_D S}{2} |\vec{v}_w - \vec{v}_T| (\vec{v}_w - \vec{v}_T) \quad (21)$$

$$\vec{F}_I = \rho C_m V_T (\vec{v}_w - \vec{v}_T) + (\rho V_T - m) \vec{v}_T \quad (22)$$

where \vec{F}_T is the wave load, \vec{F}_D is the viscous drag force term and \vec{F}_I is the inertial force term. ρ is the density of water, C_D and C_m are the drag coefficient and inertial force coefficient, respectively. \vec{v}_T and (\vec{v}_T) are the velocity and acceleration of the research object at a point, respectively. m is the mass of the research object. S is the projected area of the research object normal to the wave, and V_T is the immersed volume of the research object in the wave.

Because the motion of IPM-TENG can be decomposed into the translation of point C, followed by a rotation about the point. The following can be obtained from Newton's second law

$$\vec{F}_{D1} + \vec{F}_{I1} + F_{f1} \vec{k} - m_1 g \vec{k} + \vec{F}_{D2} + \vec{F}_{I2} + F_{f2} \vec{k} - m_2 g \vec{k} = (m_1 + m_2) \vec{a} \quad (23)$$

where \vec{F}_{D1} , \vec{F}_{I1} , $F_{f1} \vec{k}$, and $m_1 g \vec{k}$ are the drag force, the inertial force, the buoyant force, and the gravity on the floating body, respectively. \vec{F}_{D2} , \vec{F}_{I2} , $F_{f2} \vec{k}$ and $m_2 g \vec{k}$ are the drag force, the inertial force, the buoyant force, and the gravity on the assist body, respectively. \vec{a} is the acceleration of IPM-TENG. Here, the connecting rod is very light, so the weight of it can be ignored. Writing the x and z components of Eq. (23) give

$$F_{D1x} + F_{I1x} + F_{D2x} + F_{I2x} = (m_1 + m_2) \ddot{x}_0 \quad (24)$$

$$F_{D1z} + F_{I1z} + F_{f1} - m_1 g + F_{D2z} + F_{I2z} + F_{f2} - m_2 g = (m_1 + m_2) \ddot{z}_0 \quad (25)$$

where F_{D1x} , F_{I1x} , F_{D2x} and F_{I2x} are the magnitude of forces \vec{F}_{D1} , \vec{F}_{I1} , \vec{F}_{D2} and \vec{F}_{I2} components in x direction, respectively. F_{D1z} , F_{I2z} , F_{D2z} and F_{I2z} are the magnitude of forces \vec{F}_{D1} , \vec{F}_{I1} , \vec{F}_{D2} , and \vec{F}_{I2} components in z direction, respectively. \ddot{x}_0 and \ddot{z}_0 are the magnitude of the acceleration \vec{a} component in x direction, and component in z direction, respectively. The calculation of projected area and invading volume for the floating body and assist body are shown in

Supporting Information note.

The total torque of the device is

$$\vec{M} = \vec{r}_1 \times (\vec{F}_{T1} + F_{f1} \vec{k} - m_1 g \vec{k}) + \vec{r}_2 \times (\vec{F}_{T2} + F_{f2} \vec{k} - m_2 g \vec{k}) \quad (26)$$

where \vec{r}_1 and \vec{r}_2 are the arm of the net force of $\vec{F}_{T1} + F_{f1} \vec{k} + m_1 g \vec{k}$, and the net force of $\vec{F}_{T2} + F_{f2} \vec{k} + m_2 g \vec{k}$, respectively. According to the theory of rigid body rotation about a fixed axis

$$\vec{M} = J \vec{\theta} \quad (27)$$

$$J = m_1 r_1^2 + m_2 r_2^2 \quad (28)$$

where $\vec{\theta}$ is the rotational angular acceleration of the IPM-TENG about point C. And J is the moment of inertia of the IPM-TENG. The scalar form of Eq. (27) is given as

$$M = r_1(F_{D1x} + F_{f1x})\sin\theta - r_1(F_{D1z} + F_{f1z} + F_{f1} - m_1g)\cos\theta - r_2(F_{D2x} + F_{f2x})\sin\theta + r_2(F_{D2z} + F_{f2z} + F_{f2} - m_2g)\cos\theta = (m_1 r_1^2 + m_2 r_2^2) \ddot{\theta} \quad (29)$$

Based on the Runge-Kutta fourth order method and Python software, x_0 , z_0 , and θ over time can be calculated according to Eqs. (24), (25), and (29). In the initial state ($t = 0$), the research object floats on the water surface under the action of gravity and buoyancy, thus $x_0 = 0$, $\theta = \frac{\pi}{2}$, and $z_0 = \frac{H}{2} - (r_1 - a_1 + 0.0459)$, the calculation of z_0 is shown in the

Supporting Information note.

Corresponding results for IPM-TENG in the two-body mode and single-body mode are shown in Fig. S1b and Fig. S1c, respectively. For the two-body mode, the value of z_0 and θ fluctuate over time, and the amplitude of θ not exceeding 2π , which is caused by the wave of water, x_0 gradually increases because the wave travels in the positive direction of x -axis. For the single-body mode, the value of z_0 fluctuates over time, x_0 gradually increases, and θ decreases first and then increases, and the amplitude far exceeds 2π . The above results manifest that the two-body mode IPM-TENG can swing in the wave, and the single-body mode IPM-TENG always uniaxially rotates in the wave. In other words, the two-body mode IPM-TENG will be a more effective wave energy harvester. To better comprehend how the floating body moves in the IPM-TENG of the two modes, Fig. S1d-e and Fig. 2b-e describe the motion trajectory of point A within five seconds in the two modes in the x - y - z coordinate system. Here the numbers 1-5 in Fig. 2b and d indicate the period number of water wave. Under the same water wave cycle, the two modes IPM-TENG have different motion characteristics. It is obvious that the motion amplitude of two-body mode IPM-TENG is greater, and this device is an excellent candidate for high-sensitivity low-frequency wave energy harvesting.

The motion of wave is periodic, thus the control volume τ is selected to study the input energy of the wave (E_{input}), which is enclosed by the wave surface, the seabed, two planes parallel to the xoz plane with a distance of single wavelength L , and two planes parallel to the xoy plane with a distance of $2a_1$. The E_{input} within the control volume is[34].

$$\begin{aligned} E_{input} &= E_1 + E_2 = \int_{\tau(t)} \rho \frac{u^2 + v^2}{2} d\tau + \int_{\tau(t)} \rho g z d\tau \\ &= 2a_1 \int_{-\frac{L}{2}}^{\frac{L}{2}} \int_{-d}^{\eta(x,t)} \rho \left(\frac{u^2 + v^2}{2} + gz \right) dz dx \end{aligned} \quad (30)$$

where E_1 and E_2 are the kinetic and potential energy of the wave, respectively. $d\tau$ is the volume element in xyz coordinate system. d is the distance between the SWL and the seabed (Fig. S1f). The calculation result is shown in Fig. S1g, and the mean of E_{input} (\overline{E}_{input}) is equal to 105.53734 J.

The captured energy of IPM-TENG is an important metric.

$$E_t = E_p + E_h + E_v + E_r = (m_1 + m_2)gz_0 + \frac{1}{2}(m_1 + m_2)(\dot{x}_0^2 + \dot{z}_0^2) + \frac{1}{2}J\dot{\theta}^2 \quad (31)$$

where E_t is the total mechanical energy captured by the device, E_p is the potential energy, and the potential of the xoy plane is defined as zero value. E_h and E_v are the kinetic energy possessed by IPM-TENG in motion along x -axis and along z -axis, respectively. E_r is the kinetic energy of the device rotating around point C. The captured energy of the two modes IPM-TENG are all shown in Fig. 2c and e. The average of E_t (\overline{E}_t) in the two-body mode device is higher than that in the single-body mode. Which demonstrates that the two-body mode IPM-TENG can harvest wave energy more efficiently. For the two-body mode IPM-TENG, the average potential energy \overline{E}_p , the average kinetic energy along x -axis \overline{E}_h , the average kinetic energy along z -axis \overline{E}_v , the average rotational kinetic energy \overline{E}_r , and the average total mechanical energy \overline{E}_t are all listed below. $\overline{E}_p = -17.71\text{mJ}$, $\overline{E}_h = 5.85\text{mJ}$, $\overline{E}_v = 46.01\text{mJ}$, $\overline{E}_r = 10.49\text{mJ}$, and $\overline{E}_t = 44.85\text{mJ}$. The proportion of \overline{E}_p , \overline{E}_h , \overline{E}_v , \overline{E}_r are -39.03% , 13.05% , 102.57% , 23.41% , respectively. Here the position of the surface with zero potential energy will change the proportion. For the four parts of energy, the average kinetic energy along z -axis \overline{E}_v occupy the largest proportion. During the harvesting process for the kinetic energy along z -axis, according to the law of conservation of mechanical energy, the energy E_v of the nugget will be converted into potential energy and kinetic energy, and part of the potential energy will be conserved in the nugget and lower the energy conversion efficiency. Which will complex the process of calculation and experimental verification.

The conversion efficiency (η_1) of wave input energy can be expressed as:

$$\eta_1 = \frac{\overline{E}_t}{\overline{E}_{input}} \quad (32)$$

The efficiency η_1 of the two modes of IPM-TENG are 0.42%, 0.34%, respectively.

When the wave impacts the IPM-TENG in the two-body mode, parts of the input energy are transformed to the device, and most parts of energy are retained in the water, and it is defined as follows [35]:

$$E_w = E_{input} - E_t \quad (33)$$

Fig. S1h presents the retained energy of water (E_w) over time. And the mean of E_w (\overline{E}_w) is equal to 105.49249 J. Part of the mechanical energy captured by the IPM-TENG is available energy used to trigger the internal TENG units to work, and part is stored in the device. The available energy (E_a) of the IPM-TENG can be calculated as follows:

$$E_a = \frac{1}{2}m_1 \dot{x}_1^2 = \frac{1}{2}m_1 (\dot{x}_0 - r_1 \sin\theta \dot{\theta})^2 \quad (34)$$

where x_1 is the magnitude of the horizontal velocity of point A, x_0 is the magnitude of the horizontal velocity of point C, $\dot{\theta}$ is the magnitude of the angular velocity of rotation. Here the designed IPM-TENG can only harvest part energy of the captured energy of the device, and it is a demonstration for validating energy conversion model.

Fig. 2f displays the E_a of the IPM-TENG in the single-body mode and two-body mode with various lengths of connecting rod. The E_a of the single-body mode IPM-TENG are lower than the two-body mode IPM-TENG, and the average E_a (\overline{E}_a) of two-body mode IPM-TENG (connecting rod is 6 cm) is 2.39 times of the single-body mode IPM-TENG. The conversion efficiency (η_2) of mechanical energy captured by the IPM-TENG is

$$\eta_2 = \frac{\overline{E}_a}{\overline{E}_t} \quad (35)$$

The conversion efficiency η_2 of the single-body mode IPM-TENG and the two-body mode IPM-TENG are 6.65%, 12.98%, respectively.

Subsequently, the influence of wave height and frequency on the

average available energy \bar{E}_a of the two-body mode IPM-TENG were also investigated. As shown in Fig. 2g, the \bar{E}_a of IPM-TENG increases with the increase of wave height, which is due to the increase of the total input energy. As illustrated in Fig. S1i, the \bar{E}_a of IPM-TENG increases with the increase of wave frequency, however, when the wave frequency is higher than 1 Hz, there is a decreasing trend for \bar{E}_a , because the wave period is lower than the motion period of the device.

It can be seen from the above results that the conversion efficiency η_1 and η_2 of IPM-TENG can be changed by the structure and wave parameters, through the interaction of WEC and water wave.

2.3. Electric output performance and model validation

In the actual marine environment, the designed IPM-TENG can collect both the rotational energy and the horizontal motion energy. Here, a seesaw was applied to simulate and analyze the rotational state of the IPM-TENG system (Fig. 3a), and its output performance was evaluated (Fig. 3b-c and Fig. S2a). The linear motor was used to simulate the motion in horizon, and corresponding test results are displayed in Fig. 3e-f, and Fig. S2b-c. Fig. 3b presents that the open-circuit voltage (V_{OC}), the transferred charges (Q_{SC}), short-circuit current (I_{SC}) are all increase with the increase of the rotation angle of the seesaw (from 5° to 25°) in the frequency of 1 Hz. The corresponding V_{OC} , Q_{SC} , and I_{SC} increase from 123 to 240 V, 0.36–0.87 μC , and 18–42 μA , respectively. Because the increase of rotation angle of seesaw will cause the increase of separation distance and contact force of TENG units. The measured output current and peak power of IPM-TENG with varied external load resistance at different rotation angles of the seesaw are presented in Fig. S2a and Fig. 3c, respectively. The output current decreases with the increase of load resistance, and the peak power first increases and then decreases with the increase of load resistance. In addition, the output peak power has a maximum value of 12.8 mW at angle = 25° with a matched resistance of 5 $\text{M}\Omega$.

Fig. 3d describes the IPM-TENG performs linear motion driven by the

linear motor. The output Q_{SC} and I_{SC} of the IPM-TENG with different amplitudes from 2 to 10 cm and frequencies from 1 to 2 Hz are illustrated in Fig. 3e and Fig. S2b, respectively. The two all increase with the increase of amplitude and frequency. Further, the output current and peak power of the device for varied amplitudes with different external load resistances at a fixed frequency of 1 Hz are shown in Fig. S2c and Fig. 3f. Where the peak power of 20.1 mW is obtained at 5 $\text{M}\Omega$. Thus, the IPM-TENG is a candidate for efficient wave energy collection.

To validate the proposed model, a standard water tank consisting of a wave generating mechanism and a rebound wave absorber was used to generate standard water waves, which will contribute to the quantitative characterization of the IPM-TENG performance. The wave parameters include wave frequency and wave height can be controlled and adjusted by the standard water tank. The output charge of the two modes IPM-TENG are shown in Fig. 4a, the IPM-TENG in two-body mode can generate more charge compared with the single-body mode, and the average output charge of the former is 2.8 times of the latter device. Fig. 4b and Video S1 demonstrate that, under the same water wave condition, the two-body mode IPM-TENG can generate a larger amplitude of reciprocating motion and drive the same number of light-emitting diodes (96 LEDs) brighter than the single-body mode. In the meantime, 100 green LEDs can be directly driven by the two-body mode IPM-TENG at the wave height of 10 cm and wave frequency of 1 Hz (Fig. 4c).

Supplementary material related to this article can be found online at [doi:10.1016/j.nanoen.2022.107362](https://doi.org/10.1016/j.nanoen.2022.107362).

Fig. 4d-f investigated the output of IPM-TENG in two-body mode with different lengths of connecting rod and different weights of assist body, both will influence the position of COM of the device, and the corresponding schematic diagram is shown in Fig. 4e. To systematically explore the effect of the two factors, the frequency of the waves was fixed at 1 Hz and the wave height was fixed at 10 cm. The transferred charge and the average value of the transferred charge of the IPM-TENG at different lengths are depicted in Fig. 4d. As the length of the

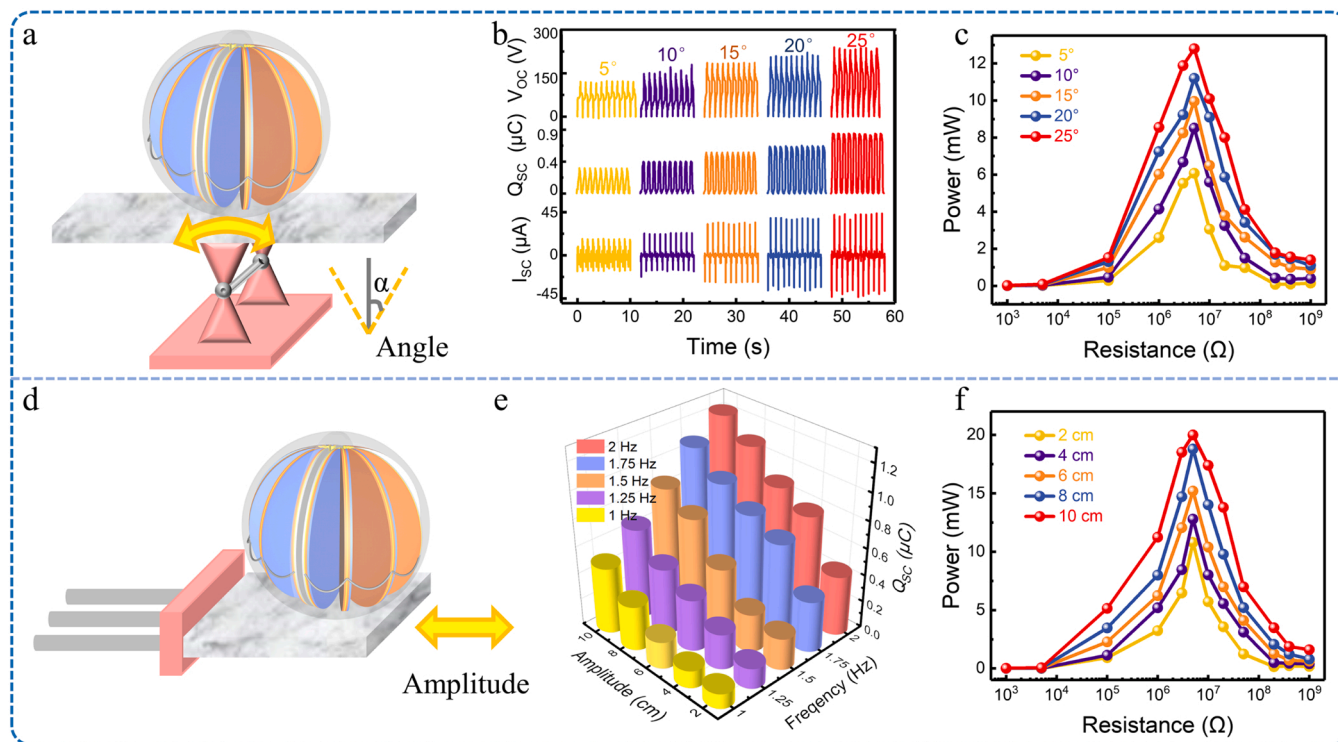


Fig. 3. Output performance of IPM-TENG by electric motor. (a) Schematic scene of IPM-TENG rotation. (b) Output performance and (c) output peak power-resistance relationship of IPM-TENG at different rotation angles at fixed frequency of 1 Hz. (d) Schematic scene of IPM-TENG translation. (e) Short-circuit charge (Q_{SC}) of IPM-TENG at various frequencies and amplitudes of linear motor. (f) Output peak power-resistance relationship of IPM-TENG under different amplitudes (1 Hz).

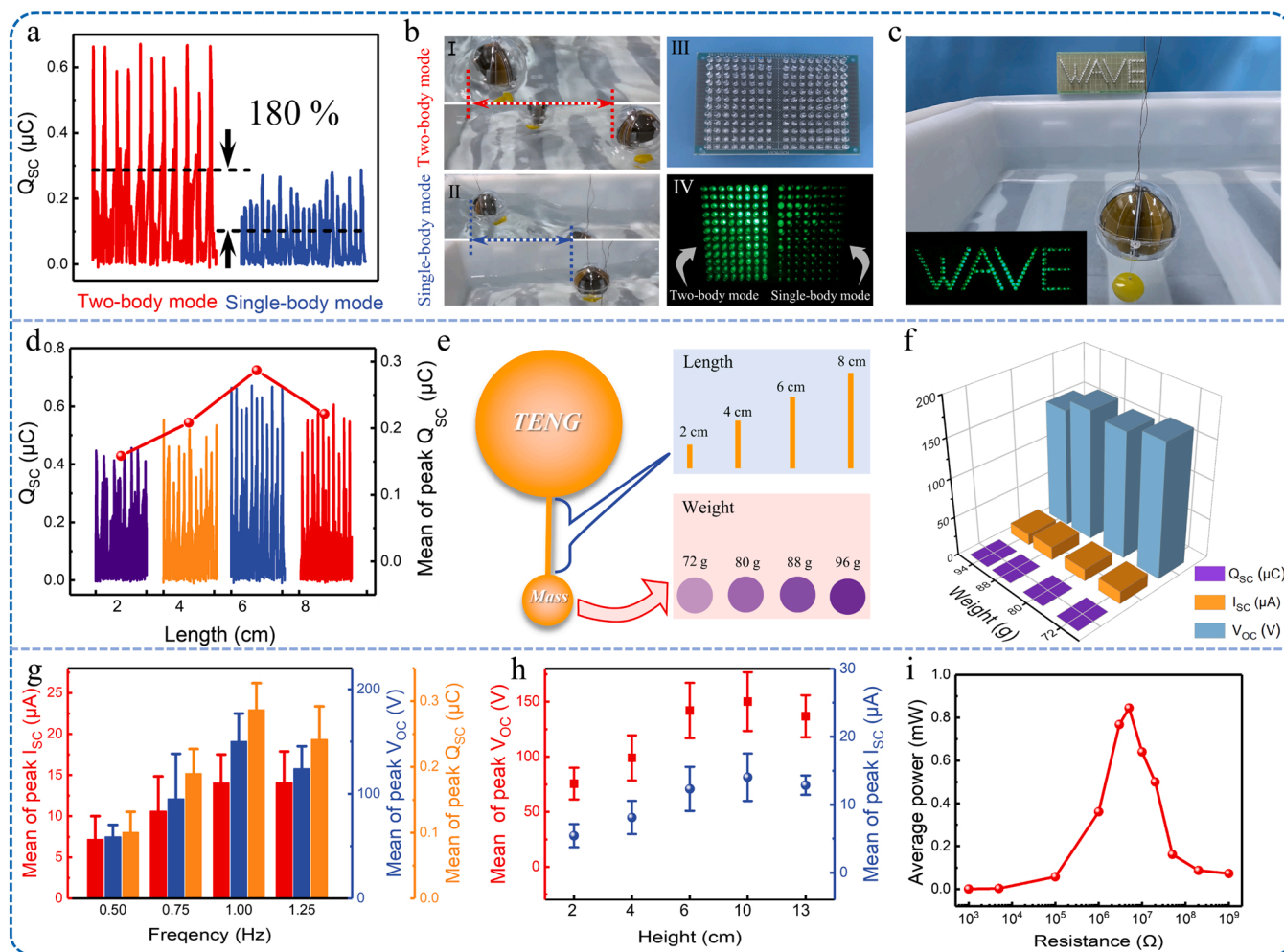


Fig. 4. Output performance of IPM-TENG in the water wave. (a) Q_{sc} of IPM-TENG in the two modes. (b) Comparison of the moving distance and powering LEDs in the two modes. (c) Picture of the IPM-TENG to power serial LEDs in “wave”. (d) Q_{sc} of IPM-TENG in the two-body mode with different lengths of connecting rod. (e) Sketches showing the connecting rods with different lengths and assist bodies with different weights in the IPM-TENG. (f) Output performance of IPM-TENG in the two-body mode with different weights of assist body. Output performance of the IPM-TENG with (g) different frequencies and (h) different heights of wave. (i) Output average power under various external loads.

connecting rod increases from 2 to 8 cm (assist body weight = 72 g), the transferred charge first increases and then decreases, which is consistent with the calculation results of energy conversion mode. When the connecting rod length is equal to 6 cm, the maximum transferred charge of the device is 0.6 μC , and the average value of the transferred charge is 0.3 μC . Fig. 4f illustrated that the output electrical performance gradually decreases with the increase of the assist body weight (from 72 to 96 g). Because the increase of the weight of the assist body causes the COM to move towards the assist body, the captured mechanical energy by the floating ball is reduced.

The electrical output performance of the two-body mode IPM-TENG system under the water wave conditions with different wave frequencies (0.5–1.25 Hz) and heights (2–13 cm) was characterized. The output performance of the IPM-TENG were measured at various wave frequencies, as demonstrated in Fig. 4g. The assist body weight was chosen as 72 g, and the wave height was fixed at 10 cm. With the increase of wave frequency, the output performance of IPM-TENG first increases and then decreases, and reaches the maximum value at 1 Hz, which is because the wave period is not enough for the nugget to fully compact the TENG units, when the wave frequency exceeds 1 Hz. The average I_{sc} and average V_{oc} increase with the increase of wave height, approximately exhibiting a linear relationship from $H = 2$ cm to $H = 10$ cm, and reaching saturated after 10 cm (Fig. 4h), which is attributed to the

amplitude of the equipment gets its limit when the wave height surpasses 10 cm. The output performance of the device tested under different structure parameters and actual wave environment is consistent with the variation tendency of the convertible energy of the floating body calculated by the energy conversion model, which proves the validity of the model.

Furthermore, an excellent environmental adaptability is also verified for IPM-TENG by measuring output charge in different solutions, including H_2O , and HCl , H_2SO_4 , NaOH , NaCl at 3.5 wt% (Fig. S3). Due to the characteristics of the IPM-TENG, the multilayer TENG units maintain 5 mm air gap with the encapsulated spherical shell, so the charges from the ionicity of the solution have little influence on the IPM-TENG.

The dependence of average power on load resistance is shown in Fig. 4i. The IPM-TENG achieves an average power of 0.845 mW at 5 M Ω external load, in a water wave with frequency of 1 Hz and height of 10 cm.

The conversion efficiency (η_3) of the available energy collected from the float to the output electrical energy of IPM-TENG is

$$\eta_3 = \frac{\overline{PT}}{E_a} = \frac{\int \overline{I^2 R} dt}{E_a} T = 14.5 \% \quad (36)$$

where \overline{P} is the average power, R is the external load resistance. The

conversion efficiency of η_1 , η_2 , η_3 of two-body mode IPM-TENG have reached 0.42%, 12.98% and 14.5%, respectively. The total wave energy transmission efficiency is calculated as

$$\eta_4 = \eta_1 \eta_2 \eta_3 \quad (37)$$

Thus improving the efficiency of each conversion process (η_1 , η_2 , η_3) is the only way to improve the wave energy conversion efficiency.

2.4. Practical application

Traditionally, plenty of pesticides are applied by spraying to control pathogens and weeds, etc., but more than 90% of them are lost into the environment during the application, which not only affects the environment and application costs, but also makes the applicator exposure to chemicals that affect health [36–41]. Here an IPM-TENG based controllable pesticide release system (ICPRS) is proposed to build self-powered smart agriculture, which can not only diminish the applicators' pesticide exposure, but also slowly release pesticides to designated locations without external energy supply. It is expected to promote the development of "precision agriculture" and optimize the use of natural resources.

The working principle and photograph of the ICPRS based on the designed IPM-TENG are displayed in Fig. 5a and Fig. 5b, respectively. The inserts of Fig. 5b show the pictures of the glyphosate-loaded carrier, and the diameter of the carrier is about 2.8 mm. The detailed fabrication process of the glyphosate-loaded carrier is exhibited in the experimental section. The two carbon paper electrodes with a distance of 16 cm at both ends of the ICPRS and the internal material form a parallel-plate capacitor with a capacitance of 35.38 pF (Fig. S4a). The AC output of IPM-TENG is connected to the electrodes of the ICPRS. The pulsed AC signal can trigger the electrostatic field between the electrodes. The glyphosate is a weak acid mixture, which can ionize in water to form hydronium ion and the conjugate base of the acid. Under the action of the electrostatic force, the conjugate base of the acid moves toward the electrode in the right to kill the weeds. The release behavior of 0.08 g glyphosate powder and glyphosate-loaded carrier containing 0.08 g

glyphosate in 300 mL of deionized water were investigated, and samples were placed within 4 cm of the left electrode. Concentrations of glyphosate at different distances from the left electrode (8, 12, 16 cm) were tested under different conditions including without external current powering, powered by direct current (DC), powered by AC for 12 h. As Fig. S4b and Fig. 5c show, when there is no current on the two electrodes, the glyphosate concentration decreases as the distance increases, which is due to the natural diffusion of glyphosate in water [42]. Under DC and AC, the glyphosate concentration all shows the trend of increases with the increase of distance. While the concentration powered by AC is higher than powered by DC, the result demonstrates the release efficiency of the system with AC is higher, because the ion can move more vigorously under AC [43,44]. The glyphosate concentrations with glyphosate-loaded carrier were lower than that with glyphosate powder at the same distance. These results imply that the ICPRS can slow release the glyphosate to the designated location preventing the rapid loss to the environment. In addition, pot experiments were applied to compare the effects of ICPRS on weeds (Fig. 5d). Fig. 5d investigated the status of weeds before and after 7 days, the results show that the changes of weed vigor were most pronounced in ICPRS powered by AC for 12 h compared to the weed without power supply. Therefore, ICPRS can effectively control the on-demand release of pesticides and is expected to promote the development of a self-powered smart agricultural system.

3. Conclusion

In this work, a two-body mode IPM-TENG has been proposed to harvest water wave energy. Starting from the theory of hydromechanics, an energy conversion model was proposed to investigate the hydrodynamic performance and energy conversion mechanism in the process of interaction between liquid fluid and solid. According to the model, various structural parameters and wave conditions were studied in-depth theoretically and experimentally, and the results of the two were consistent. The mechanical energy capture efficiency of IPM-TENG, the ratio of the available energy of IPM-TENG to the captured mechanical energy, and the conversion efficiency of the available energy

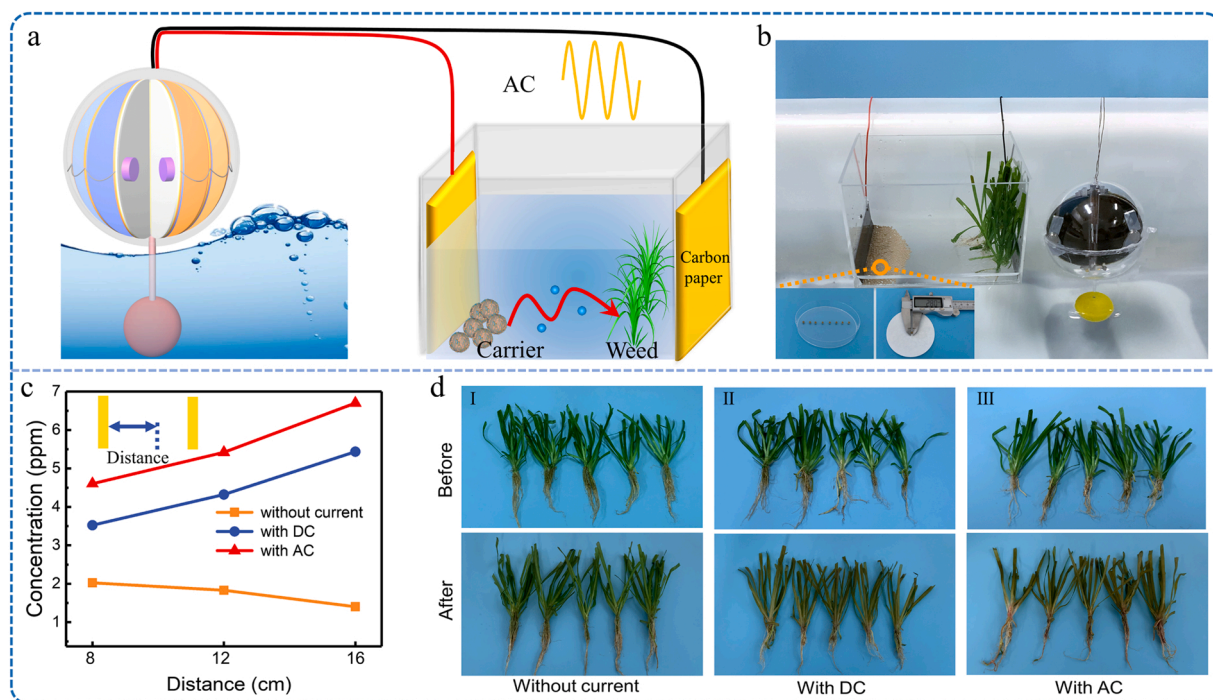


Fig. 5. Controlled release of herbicides in TENG electric field. (a) 3D schematic and (b) photo of the experimental setup and protocol. (c) The concentration distribution of herbicide in different positions on condition of without current, with AC, and with DC. (d) The pictures of weeds before and 7 days after reaction under different conditions.

into electrical energy were 0.42%, 12.98%, and 14.5%, respectively. To boost the total conversion efficiency of wave energy into electrical energy, it is necessary to improve the three conversion efficiencies mentioned above. The constructed energy conversion model pointed out the direction of the design, optimization, and improvement of wave energy harvesting efficiency of future W-TENG. In addition, the constructed IPM-TENG based controllable pesticide release system can promote the development of “precision agriculture”.

4. Experiment section

4.1. Materials

Herein, glyphosate powder, calcium chloride (CaCl_2), sodium alginate were bought from Aladdin. Attapulgite powder (particle size: 200 mesh) was purchased from Mingmei Co., Ltd. (Anhui, China).

4.2. Fabrication of IPM-TENG

Fold the paper into a zigzag shape with 6 small parts and cut it into a semicircle with a radius of 4 cm. Stick polytetrafluoroethylene film (thickness: 0.03 mm) and aluminum film (thickness: 0.03 mm) on one side of the paper and stick the other side together with Kapton tape to form a contact-separated mode multilayer TENG with three pairs of basic units. The edges of the multilayer TENG were connected by cords. Divide the acrylic spherical shell (diameter: 10 cm) into two identical spaces by an acrylic sheet with foam (thickness: 1 mm) on both sides. One side of the multilayer TENG was fixed on the foam of acrylic sheet. On the other side of a multi-layer TENG basic unit, there existed semi-circular acrylic sheet (radius: 4 cm) pasted with foam (thickness 1 mm) and nugget (weight: 17 g) to increase the contacting efficiency of the TENG. So far, the floating body including four TENG basic units and an acrylic spherical shell was completed. Connect the floating ball to the acrylic connecting rod (diameter: 3 mm, length: 6 cm) and assist body (diameter: 4 cm, weight: 72 g) with waterproof glue to assemble a two-body mode IPM-TENG. Directly connect the floating ball and the assist ball with waterproof glue, thus a single-body mode generator was completed.

4.3. Preparation of glyphosate-loaded carrier

Disperse attapulgite powder (particle size: 200 mesh, weight: 0.8 g) and glyphosate powder (weight: 0.08 g) in 16 mL deionized water, and then stir (500 rpm) the resulting system for 30 min with magnetic stirrer. Sodium alginate (weight: 0.2 g) was added into the mixed solution, and then the mixture was stirred (500 rpm) for 30 min to form a homogeneous suspension. A syringe (needle diameter: 1 mm) was used to dropwise inject the homogeneous suspension into 40 mL CaCl_2 solution (mass-volume percent: 0.5%), and the glyphosate-loaded carrier spheres with the diameter of 1–2 mm were obtained. Finally, wash the formed carrier spheres 5 times with deionized water.

4.4. Electric measurements of the TENG device

All devices were triggered by a seesaw, linear motor, or regular water wave generated by the wave tank. The open-circuit voltage, short-circuit current, the short-circuit charge were measured by the electrometer (Keithley 6514.).

Declaration of Competing Interest

The authors declare that they have no known competing financial interests or personal relationships that could have appeared to influence the work reported in this paper.

Acknowledgments

This work was supported by the National Key R & D Project from Minister of Science and Technology (2021YFA1201602), the National Natural Science Foundation of Chongqing (cstc2019jcyj-msxmX0068), National Natural Science Foundation of China (NSFC) (U21A20147, 52073037), Fundamental Research Funds for the Central Universities (Grant No. 2021CDJQY-005). The authors would like to thank Analytical and Testing Center of Chongqing University for some electrode preparations and material characterizations.

Appendix A. Supporting information

Supplementary data associated with this article can be found in the online version at [doi:10.1016/j.nanoen.2022.107362](https://doi.org/10.1016/j.nanoen.2022.107362).

References

- [1] T. Bhatta, P. Maharjan, K. Shrestha, S. Lee, M. Salauddin, M.T. Rahman, S.M. S. Rana, S. Sharma, C. Park, S.H. Yoon, J.Y. Park, A hybrid self-powered arbitrary wave motion sensing system for real-time wireless marine environment monitoring application, *Adv. Energy Mater.* 12 (2021).
- [2] Y. Feng, J. Han, M. Xu, X. Liang, T. Jiang, H. Li, Z.L. Wang, Blue energy for green hydrogen fuel: a self-powered electrochemical conversion system driven by triboelectric nanogenerators, *Adv. Energy Mater.* 12 (2021).
- [3] C. Rodrigues, D. Nunes, D. Clemente, N. Mathias, J.M. Correia, P. Rosa-Santos, F. Taveira-Pinto, T. Morais, A. Pereira, J. Ventura, Emerging triboelectric nanogenerators for ocean wave energy harvesting: state of the art and future perspectives, *Energy Environ. Sci.* 13 (2020) 2657–2683.
- [4] X. Chen, L. Gao, J. Chen, S. Lu, H. Zhou, T. Wang, A. Wang, Z. Zhang, S. Guo, X. Mu, Z.L. Wang, Y. Yang, A chaotic pendulum triboelectric-electromagnetic hybridized nanogenerator for wave energy scavenging and self-powered wireless sensing system, *Nano Energy* 69 (2020).
- [5] S.-F. Leung, H.-C. Fu, M. Zhang, A.H. Hassan, T. Jiang, K.N. Salama, Z.L. Wang, J.-H. He, Blue energy fuels: converting ocean wave energy to carbon-based liquid fuels via CO_2 reduction, *Energy Environ. Sci.* 13 (2020) 1300–1308.
- [6] Z. Ren, X. Liang, D. Liu, X. Li, J. Ping, Z. Wang, Z.L. Wang, Water-wave driven route avoidance warning system for wireless ocean navigation, *Adv. Energy Mater.* 11 (2021).
- [7] J. Han, Y. Feng, P. Chen, X. Liang, H. Pang, T. Jiang, Z.L. Wang, Wind-driven soft-contact rotary triboelectric nanogenerator based on rabbit fur with high performance and durability for smart farming, *Adv. Funct. Mater.* 32 (2021).
- [8] J.S. Kim, J. Kim, J.N. Kim, J. Ahn, J.H. Jeong, I. Park, D. Kim, I.K. Oh, Collectively exhaustive hybrid triboelectric nanogenerator based on flow-induced impacting-sliding cylinder for ocean energy harvesting, *Adv. Energy Mater.* 12 (2021).
- [9] S. Fu, W. He, Q. Tang, Z. Wang, W. Liu, Q. Li, C. Shan, L. Long, C. Hu, H. Liu, An ultrarobust and high-performance rotational hydrodynamic triboelectric nanogenerator enabled by automatic mode switching and charge excitation, *Adv. Mater.* 34 (2022), e2105882.
- [10] X. Liang, Z. Liu, Y. Feng, J. Han, L. Li, J. An, P. Chen, T. Jiang, Z.L. Wang, Spherical triboelectric nanogenerator based on spring-assisted swing structure for effective water wave energy harvesting, *Nano Energy* 83 (2021).
- [11] X. Zhang, J. Hu, Q. Yang, H. Yang, H. Yang, Q. Li, X. Li, C. Hu, Y. Xi, Z.L. Wang, Harvesting multidirectional breeze energy and self-powered intelligent fire detection systems based on triboelectric nanogenerator and fluid-dynamic modeling, *Adv. Funct. Mater.* 31 (2021).
- [12] X. Zhang, J. Hu, Q. Zeng, H. Yang, W. He, Q. Li, X. Li, H. Yang, C. Hu, Y. Xi, A non-encapsulated polymorphous u-shaped triboelectric nanogenerator for multiform hydropower harvesting, *Adv. Mater. Technol.* 6 (2021).
- [13] C. Chen, Z. Wen, J. Shi, X. Jian, P. Li, J.T.W. Yeow, X. Sun, Micro triboelectric ultrasonic device for acoustic energy transfer and signal communication, *Nat. Commun.* 11 (2020).
- [14] Y. Chen, Z. Gao, F. Zhang, Z. Wen, X. Sun, Recent progress in self-powered multifunctional e-skin for advanced applications, *Exploration* 2 (2022), 20210112.
- [15] H. Lei, Y. Chen, Z. Gao, Z. Wen, X. Sun, Advances in self-powered triboelectric pressure sensors, *J. Mater. Chem. A* 9 (2021) 20100–20130.
- [16] X. Liang, T. Jiang, Y. Feng, P. Lu, J. An, Z.L. Wang, Triboelectric nanogenerator network integrated with charge excitation circuit for effective water wave energy harvesting, *Adv. Energy Mater.* 10 (2020).
- [17] Z. Lin, B. Zhang, Y. Xie, Z. Wu, J. Yang, Z.L. Wang, Elastic-connection and soft-contact triboelectric nanogenerator with superior durability and efficiency, *Adv. Funct. Mater.* 31 (2021).
- [18] C. Zhang, L. He, L. Zhou, O. Yang, W. Yuan, X. Wei, Y. Liu, L. Lu, J. Wang, Z. L. Wang, Active resonance triboelectric nanogenerator for harvesting omnidirectional water-wave energy, *Joule* 5 (2021) 1613–1623.
- [19] X. Liang, T. Jiang, G. Liu, Y. Feng, C. Zhang, Z.L. Wang, Spherical triboelectric nanogenerator integrated with power management module for harvesting multidirectional water wave energy, *Energy Environ. Sci.* 13 (2020) 277–285.
- [20] H. Pang, Y. Feng, J. An, P. Chen, J. Han, T. Jiang, Z.L. Wang, Segmented swing-structured fur-based triboelectric nanogenerator for harvesting blue energy toward marine environmental applications, *Adv. Funct. Mater.* 31 (2021).

- [21] H. Wu, Z. Wang, Y. Zi, Multi-mode water tube based triboelectric nanogenerator designed for low-frequency energy harvesting with ultrahigh volumetric charge density, *Adv. Energy Mater.* 11 (2021).
- [22] S. Xu, G. Liu, J. Wang, H. Wen, S. Cao, H. Yao, L. Wan, Z.L. Wang, Interaction between water wave and geometrical structures of floating triboelectric nanogenerators, *Adv. Energy Mater.* 12 (2021).
- [23] Y. Wang, A.T.T. Pham, X. Han, D. Du, Y. Tang, Design and evaluate the wave driven-triboelectric nanogenerator under external wave parameters: experiment and simulation, *Nano Energy* 93 (2022).
- [24] K. Budar, J. Falnes, A resonant point absorber of ocean-wave power, *Nature* 256 (1975) 478–479.
- [25] A.F.O. Falcão, J.C.C. Henriques, Oscillating-water-column wave energy converters and air turbines: a review, *Renew. Energy* 85 (2016) 1391–1424.
- [26] B.-H. Kim, J. Wata, M.A. Zullah, M.R. Ahmed, Y.-H. Lee, Numerical and experimental studies on the PTO system of a novel floating wave energy converter, *Renew. Energy* 79 (2015) 111–121.
- [27] H. Xiao, M. Pan, J.Y.H. Chu, C.R. Bowen, S. Bader, J. Aranda, M. Zhu, Hydraulic pressure ripple energy harvesting: structures, materials, and applications, *Adv. Energy Mater.* (2022).
- [28] Y. Wang, C. Zhong, S. Liu, Arbitrary lagrangian-eulerian-type discrete unified gas kinetic scheme for low-speed continuum and rarefied flow simulations with moving boundaries, *Phys. Rev. E* 100 (2019), 063310.
- [29] B. Dorschner, S.S. Chikatamarla, I.V. Karlin, Fluid-structure interaction with the entropic lattice Boltzmann method, *Phys. Rev. E* 97 (2018), 023305.
- [30] S. Fu, Y. Tsur, J. Zhou, L. Shemer, A. Arie, Propagation dynamics of airy water-wave pulses, *Phys. Rev. Lett.* 115 (2015), 034501.
- [31] G. Dematteis, T. Grafke, M. Onorato, E. Vanden-Eijnden, Experimental evidence of hydrodynamic instantons: the universal route to rogue waves, *Phys. Rev. X* 9 (2019).
- [32] J. Wienke, H. Oumeraci, Breaking wave impact force on a vertical and inclined slender pile—theoretical and large-scale model investigations, *Coast. Eng.* 52 (2005) 435–462.
- [33] S. Fatehboroujeni, A. Gopinath, S. Goyal, Three-dimensional nonlinear dynamics of prestressed active filaments: flapping, swirling, and flipping, *Phys. Rev. E* 103 (2021), 013005.
- [34] P. Cobelli, A. Pradzka, P. Petitjeans, G. Lagubeau, V. Pagneux, Different regimes for water wave turbulence. A. Maurel, *Phys. Rev. Lett.* 107 (2011), 214503.
- [35] A. Costa, A.R. Osborne, D.T. Resio, S. Alessio, E. Chrivi, E. Saggese, K. Bellomo, C. E. Long, Soliton turbulence in shallow water ocean surface waves, *Phys. Rev. Lett.* 113 (2014), 108501.
- [36] V. Ghormade, M.V. Deshpande, K.M. Paknikar, Perspectives for nano-biotechnology enabled protection and nutrition of plants, *Biotechnol. Adv.* 29 (2011) 792–803.
- [37] T. Liu, J. Luo, S. Liu, T. Li, H. Li, L. Zhang, W. Mu, N. Zou, Clothianidin loaded TA/Fe (III) controlled-release granules: improve pesticide bioavailability and alleviate oxidative stress, *J. Hazard. Mater.* 416 (2021), 125861.
- [38] M. Nuruzzaman, M.M. Rahman, Y. Liu, R. Naidu, Nano-guard for pesticides: a new window for safe application, *J. Agric. Food Chem.* 64 (2016) 1447–1483.
- [39] P. Wang, E. Lombi, F.J. Zhao, P.M. Kopittke, Nanotechnology: a new opportunity in plant sciences, *Trends Plant Sci.* 21 (2016) 699–712.
- [40] L. Zhang, S. Ren, C. Chen, D. Wang, B. Liu, D. Cai, Z. Wu, Near infrared light-driven release of pesticide with magnetic collectability using gel-based nanocomposite, *Chem. Eng. J.* 411 (2021).
- [41] X. Zhao, H. Cui, Y. Wang, C. Sun, B. Cui, Z. Zeng, Development strategies and prospects of nano-based smart pesticide formulation, *J. Agric. Food Chem.* 66 (2018) 6504–6512.
- [42] L. Zhang, C. Chen, G. Zhang, B. Liu, Z. Wu, D. Cai, Electrical-driven release and migration of herbicide using a gel-based nanocomposite, *J. Agric. Food Chem.* 68 (2020) 1536–1545.
- [43] Z. Tang, S. Lin, Z.L. Wang, Quantifying contact-electrification induced charge transfer on a liquid droplet after contacting with a liquid or solid, *Adv. Mater.* 33 (2021), e2102886.
- [44] X. Sun, Y. Feng, B. Wang, Y. Liu, Z. Wu, D. Yang, Y. Zheng, J. Peng, M. Feng, D. Wang, A new method for the electrostatic manipulation of droplet movement by triboelectric nanogenerator, *Nano Energy* 86 (2021).



Xuemei Zhang received her B.S. degree in physics from Chongqing Normal University in 2019. Now she is a post-graduate student in Chongqing University. Her current research is triboelectric nanogenerator.



Qianxi Yang received his B.S degree in Theoretical Physics from Chongqing University in 2020. Now he is a postgraduate student in Chongqing University. His current research focuses on triboelectric nanogenerator sensor.



Peiyuan Ji is a Ph.D. student in physics, Chongqing University, China. His current research focuses on the conversion and storage integration of high entropy energy.



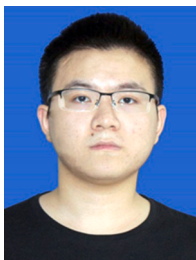
Zhifei Wu received his B.S. degree in Physics(2020) from Chongqing University. Now he is a master in the field of Physics, Chongqing University. Currently, his research interests are mainly focused on perturbative QCD.



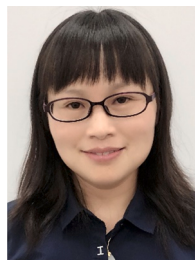
Qianying Li received her B.S. degree in Physics from Chongqing Technology and Business University in 2018. Now, she is a PhD student in the field of Physics, Chongqing University. Currently, her research interests are mainly focused on TENG-based high voltage technology.



Huake Yang received his B.S. degree in Applied Physics (2017) and M.S. degree in Physics (2020) from Chongqing University. Now, he is a Ph.D. student at Chongqing University. His research interests are mainly focused on triboelectric nanogenerator.



Xiaochuan Li received his B.S. degree in Applied Physics from Chongqing University in 2019. Now, he is a PhD student in the field of physics, Chongqing University. His current research is triboelectric nanogenerators for energy harvesting.



Yi Xi is now a professor at Chongqing University, China. She received her Ph.D. degree in Physics from Chongqing University in 2010. Her main research interests focus on the fields piezoelectric, triboelectric nanogenerators for energy harvesting and supercapacitors for energy storage, self-powered sensor system. She is the author of more than 150 publications and holds more than 10 patents.



Guocan Zheng is a senior engineer in Analytical and Testing Center of Chongqing University, China. He has been engaged in the research of mass spectrometry and chromatographic analysis and detection technology.



Prof. Zhong Lin Wang received his Ph.D. from Arizona State University in physics. He now is the Hightower Chair in Materials Science and Engineering, Regents' Professor, Engineering Distinguished Professor and Director, Center for Nanostructure Characterization, at Georgia Tech. Prof. Wang has made original and innovative contributions to the synthesis, discovery, characterization and understanding of fundamental physical properties of oxide nanobelts and nanowires, as well as applications of nanowires in energy sciences, electronics, optoelectronics and biological science. His discovery and breakthroughs in developing nanogenerators established the principle and technological road map for harvesting

mechanical energy from environment and biological systems for powering a personal electronics. His research on self-powered nanosystems has inspired the worldwide effort in academia and industry for studying energy for micro-nano-systems, which is now a distinct disciplinary in energy research and future sensor networks. He coined and pioneered the field of piezotronics and piezo-phototronics by introducing piezoelectric potential gated charge transport process in fabricating new electronic and optoelectronic devices.